Optimization of fluorinated interfacial layers with minimal surface coverage for hybrid perovskite materials

Riva Alkarsifi, Thierry Buffeteau, Christine Labrugère-Sarroste, Lionel Hirsch, Dario M Bassani, Thierry Toupance

Optimization of fluorinated interfacial layers with minimal surface coverage for hybrid perovskite materials

Riva Alkarsifi,[†§] Thierry Buffeteau,[†] Christine Labrugère-Sarroste,[‡] Lionel Hirsch,[§] Dario M. Bassani[†*] and Thierry Toupance[†*]

† Univ. Bordeaux, CNRS, Bordeaux INP, ISM, UMR 5255, F-33400 Talence, France

‡ Univ. Bordeaux, CNRS, PLACAMAT, UAR 3626, F-33600 Pessac, France

§ Univ. Bordeaux, IMS, CNRS, UMR 5218, Bordeaux INP, ENSCBP, F-33400 Talence, France

ABSTRACT: The efficiency of fluorinated interfacial adlayers exhibiting minimal surface coverage in protecting and tuning the electronic properties of hybrid perovskite materials is optimized using a combination of XPS, Kelvin probe, and contact angle measurements to characterize the composition, surface potential, and wettability. Results are interpreted on the basis of photoluminescence quantum efficiency (PLQE) and time-resolved luminescence to assess the adlayer's effect on non-radiative charge recombination. Polarization-modulation infrared reflection absorption spectroscopy reveals that for the tetra(fluoroalkyl)stannanes and chlorotri(fluoroalkyl)stannanes studied, the wettability and work function of the modified surfaces are the result of the organization of the adlayer's molecular components and their propensity to selectively passivate defects. For some cases, the effect of solvent choice for the deposition can play a more significant role than modifying the adlayer’s thickness or chemical

composition. Our results show that the surface potential of methylammonium lead triiodide can be tuned over a 230 mV range using a mono-molecular adlayer of chlorotri(fluoroalkyl)stannane whereas the tetra(fluoroalkyl)stannanes provide the strongest hydrophobicity (contact angle > 80°) with little change in the surface potential. The solvent used for deposition strongly affects the molecular organization and net dipole moment, leading to significant variations in the surface coverage and the electronic properties of the perovskite surface. Whereas exposing the methylammonium lead triiodide (MAPI) surface to neat solvent results in a change in surface properties, only the presence of interfacial layers resulted in an enhancement of the PLQE that is proportional to the average PL lifetime, irrespective of the formation of a compact monolayer.

KEYWORDS: fluorinated compounds, perovskite films, adlayers, surface engineering, passivation

INTRODUCTION

The rapid development of perovskite solar cells (PSCs) over the past decade is a result of their fundamental optoelectronic properties, which include high absorption covering the entire visible region,[1] tunable direct bandgap ~1.55 to 2.50 eV,[2] high charge carrier mobility,[3] fast exciton dissociation, and long charge carrier diffusion lengths, combined with low-cost solution processing.[4] At present, the certified power conversion efficiency (PCE) for a single-junction perovskite solar cell has reached 26%.[5] Despite this tremendous increase in the overall PCE, the use of PSCs is limited by issues related to their long-term device stability.[6] The polycrystalline nature of the solution-processed perovskite films results in structural disorder, such as grain boundary defects and crystallographic defects in the form of vacancies, interstitials, and antisite substitutions. These defects in the bulk and/or at the surface can trigger degradation of the

perovskite film, thus reducing device stability. To alleviate this and further improve the electronic properties of the material, surface passivation is actively pursued as a promising route to reduce the non-radiative recombination losses and further boost device performance and stability.[7-9] These, however, must reconcile adequate modification of the surface properties while not impairing electrical connectivity with the electrodes resulting from the presence of a thick or electrically insulating layer.

Numerous passivating agents for perovskite materials have been developed, including Lewis acid/base additives and zwitterions,[10,11] that play several roles, including passivating defects, modifying the interfacial electronic properties, or offering moisture protection. A Lewis acid may passivate negatively charged defects, thus eliminating trap states.[6,12] For instance, tris(pentafluorophenyl) phosphine (TPFP) was used as a strong Lewis acid to passivate halide defects, resulting in an enhancement of the V_{OC} and PCE (from 18.05% to 21.04%).[13] In contrast, Lewis bases such as pyridine or thiophene derivatives may passivate positively charged defects.[14-16] Functional groups with lone pairs, such as carboxylates and phosphoric acid containing C=O and P=O groups, show similar defect passivation effects.[17] Other than Lewis acids and bases, zwitterions have been proposed to passivate trap states by forming ionic bonds with point defects.[11,18] Jiang et *al.*[7] reported the incorporation of phenethylammonium iodide (PEAI) as a surface modifier. This passivation reduced the density of defects on mixed perovskite films and suppressed non-radiative recombination, resulting in a certified PCE of 23.32%.

The surface of hybrid organic-inorganic perovskite (HOIP) materials easily absorbs moisture owing to the ionic nature of the perovskite crystal, and this can result in its degradation to PbI_2.[19] To overcome this issue and improve the device stability, numerous groups incorporated

molecules capable of forming a compact hydrophobic layer on the perovskite surface.[20-22] To this end, the use of bulky alkyl chains[23] or hydrophobic aromatic compounds[24] was found to enhance device stability. In particular, fluorocarbons are well suited due to their strong hydrophobicity and possible binding interactions with the perovskite surface. Functionalization with fluorinated groups was found to significantly modify the hydrophobicity and the surface potential of the active perovskite layer resulting in improved air stability.[6] Using polarization modulation-infrared absorption reflection spectroscopy (PM-IRRAS), Sadhu *et al.* showed that unsubstituted perfluoro-*n*-alkanes could weakly bond to a MAPI surface, forming stable monolayers with well-defined orientation.[25] The interactions between the perfluorinated compounds and the perovskite surface also alter the electronic properties of the MAPI surface, leading to a change in the surface work function (WF) over a 150-mV range. This can considerably affect the performance of PSC devices through energy level (mis)matching between the active layer and the electrode and represents an entry into tuning the surface properties.

Numerous recent studies have revealed that the structure – activity relationship in perovskite surface passivating agents is much more complex than previously thought,[26-30] and that the modification of the electronic properties or operational lifetime may result from effects that are specific to individual systems.[31,32] For example, when comparing the effect of 4-fluorophenethylammonium iodide (F-PEAI)[33] with its non-fluorinated analogue (PEAI),[7] it was observed that F-PEAI-treated devices show enhanced stability by maintaining 90% of their initial efficiency after 720 h of exposure to humidity.[33] This effect was assigned to the increased hydrophobicity of the fluorinated compound even though its fluorine content represents < 15 % *w/w*. Later studies instead showed that F-PEAI is organized vertically on the perovskite surface, forming compact monolayers. In contrast, PEAI is oriented horizontally and possesses a much

smaller surface coverage. Thus, the difference in surface coverage is likely responsible for the improved performance of F-PEAI-treated devices.[34] Additionally, different molecular orientations can result in different surface dipoles that may modify defect passivation mechanisms and surface work function.[35,36]

Despite the great interest in improving the performance of PSC devices using interfacial layers, few studies investigated how the interaction between an adlayer and the perovskite material affects the material's electronic properties and hydrophobicity. To improve our understanding of how adlayers contribute to modifying the interfacial properties of HOIPs with the intention of passivating the perovskite surface, we turned our attention to fluorinated compounds as they are currently lead compounds for perovskite surface passivation. In particular, perfluoro organotin Lewis acids with a tetrahedral geometry seem promising as they are generally air-stable and can contribute to modifying both the electronic properties and surface hydrophobicity. Herein, R_4Sn and R_3SnCl derivatives having different molecular dipole moments, along with commercially-available tri(pentafluorophenyl)borane, (Figure 1) were used to form interfacial layers on top of a MAPI perovskite surface and their effect on hydrophobicity, luminescence, and work function was evaluated using contact angle (CA), steady-state/time-resolved photoluminescence and Kelvin probe measurements, respectively. Additionally, the chemical composition of the adlayer, its thickness, and molecular orientations were characterized using X-ray diffraction (XRD), X-ray photoelectron spectroscopy (XPS), and PM-IRRAS. The results highlight how chemically engineering the composition and the net dipole of the adlayer can modify the perovskite work function and hence the electrical behavior of the active layer. Surprisingly, although noticeable differences can be found for similar molecules having different chain lengths, an even more significant effect is observed for some compounds when these are

deposited from different solvents (toluene vs. α,α,α-trifluorotoluene). This can lead to essential variations in surface potential (over 200 mV) and contact angle, which may contribute to the lack of consensus over some interfacial layer's efficiency (or lack thereof). Importantly, we find that non-radiative recombination is significantly reduced even after only partial surface coverage by fluorinated adlayers, indicative of substantial surface passivation through site-specific interactions.

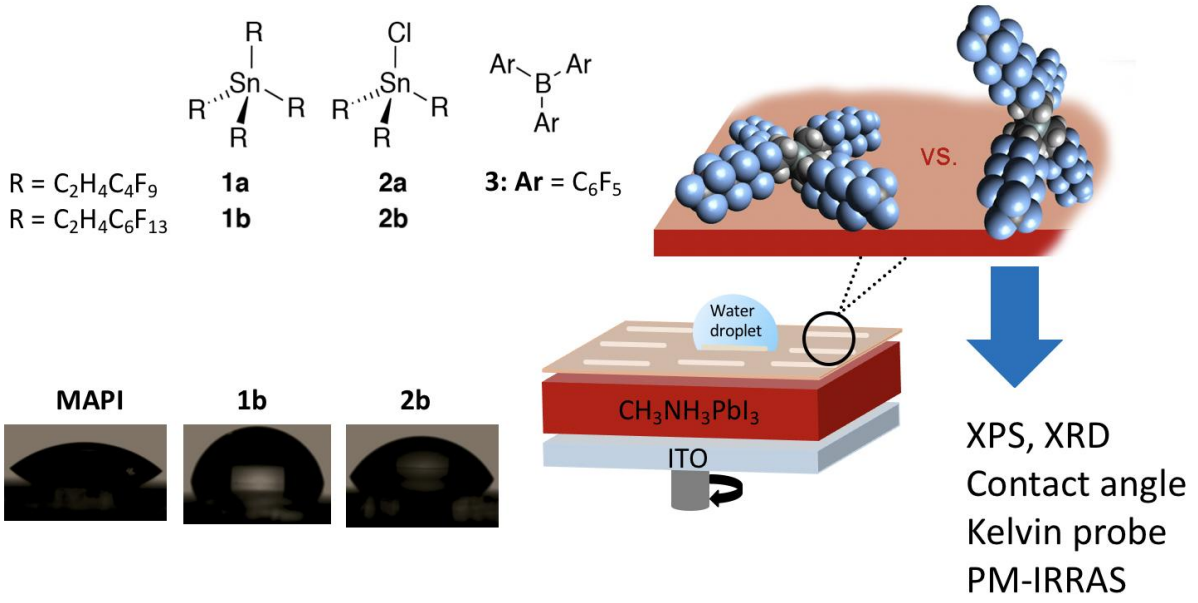

Figure 1. Chemical structures of the fluorinated surface adlayers for MAPI perovskite materials. The deposition of the adlayer was achieved by spin-coating a 10 mM solution (100µL) of **1**, **2**, or **3** in toluene or α,α,α-trifluorotoluene, followed by rinsing with pure solvent. Bottom: optical photographs of the contact angle of a water droplet on a MAPI surface in the absence or presence of a molecular layer of **1b** or **2b**. The energy minimized (MMFF94) structures of **1b** oriented horizontal or perpendicular to the perovskite surface are presented.

EXPERIMENTAL METHODS

Synthesis of $(C_4F_9C_2H_4)_4Sn$ (1a). A Grignard reagent was prepared by stirring a mixture of magnesium turnings (30 mmol, 0.73 g) in dry Et_2O (30 mL) for 1 h at ambient temperature and under nitrogen. A solution of $C_4F_9C_2H_4I$ (9.34 g, 25 mmol) in dry Et_2O (30 mL) with two drops of 1,2-dibromoethane was slowly added at 0°C. The reaction mixture was stirred for 3 h at this temperature before dry Et_2O (30 mL) was added. $SnCl_4$ (1.3 g, 5 mmol) dissolved in dry toluene (20 mL) was added dropwise, after which the mixture was heated under reflux for 4 days. The reaction was hydrolyzed by the slow addition of water (30 mL) and the mixture was filtered through Celite and then washed with pentane. The filtrates were extracted with ethyl acetate. The organic phase was washed twice with water, dried over $MgSO_4$, and concentrated by rotary evaporation. The crude product was finally purified by the classical column chromatography on silica gel using hexane as an eluent to give pure **1a** (42% yield) as a colorless oil.

^{1}H NMR (300.2 MHz, $CDCl_3$) δ 1.12 (t, 8H, $^3J_{H–H}$ = 8 Hz, $^2J_{Sn–H}$ = 52 Hz), 2.29 (tt, 8H, $^3J_{F–H}$ = 18 Hz, $^3J_{H–H}$ = 8 Hz); ^{19}F NMR (282.4 MHz, $CDCl_3$) δ − 81.14 (t, 12F), −116.96 (m, 8F), −124.60 (m, 8F), −126.13 (m, 8F); ^{13}C NMR (75 MHz, $CDCl_3$) δ -1.81 (s, $^1J_{C–Sn}$ = 170 Hz), 27.31 (t, $^2J_{C–F}$ = 23 Hz); ^{119}Sn NMR (223.8 MHz, $CDCl_3$) δ 10.83.

HRMS (ESI^-) m/z theoretical for $C_{24}H_{16}ClF_{36}Sn$ = 1142.9393, found $[M+Cl]^-$ = 1142.9362.

Synthesis of $(C_4F_9C_2H_4)_3SnCl$ (2a). Phenyltin trichloride (1.87 g, 6.22 mmol) solution in dry toluene (12 mL) was added dropwise to the Grignard reagent $C_4F_9C_2H_4MgI$, prepared as previously mentioned. The reaction mixture was refluxed for 4 h and stirred overnight at ambient temperature. The reaction was hydrolyzed by the slow addition of NH_4Cl solution and then filtrated through a Celite pad. The organic phase was washed with 5% $Na_2S_20_3$ solution and deionized water, dried over $MgSO_4$, and concentrated by rotary evaporation. The crude product

was finally purified by the classical column chromatography on silica gel using hexane to give $(C_4F_9C_2H_4)_3SnPh$ (65.1% yield) as a colorless oil.

^{1}H NMR (300.2 MHz, $CDCl_3$) δ 1.30 (t, 6H, $^3J_{H–H}$ = 8 Hz, $^2J_{Sn–H}$ = 55 Hz), 2.31 (tt, 6H, $^3J_{F–H}$ = 18 Hz, $^3J_{H–H}$ = 8 Hz), 7.4 (m, *5* H); ^{19}F NMR (282.4 MHz, $CDCl_3$) δ – 81.22 (t, 9F), −116.88 (m, 6F), −124.48 (m, 6F), −126.19 (m, 6F); ^{13}C NMR (75 MHz, $CDCl_3$) δ -1.66 (s, $^1J_{C–Sn}$ = 170 Hz), 27.54 (t, $^2J_{C–F}$ = 23 Hz), 136.23 (1C, quaternary), 135.96 (2C, $^2J_{Sn-C}$ = 17 Hz), 129.55 (1C, $^4J_{Sn-C}$ = 6 Hz), 128.96 (2C, $^3J_{Sn-C}$ = 25 Hz); ^{119}Sn NMR (223.8 MHz, $CDCl_3$) δ -33.59.

Trimethylsilyl chloride TMSCl (7.5 mmol, 0.95 mL) was added at 0 °C to a carbon tetrachloride CCl_4 solution (15 mL) containing $(C_4F_9C_2H_4)_3SnPh$ (5 mmol, 4.69 g) and dry MeOH (25 mmol, 1 mL). The reaction mixture was stirred overnight at ambient temperature. The solution was evaporated, and the crude product was subjected to column chromatography on silica gel using dichloromethane as an eluent to give **2a** (5.49 g, 46.8%).

^{1}H NMR (300.2 MHz, $CDCl_3$) δ 1.52 (t, 6H, $^3J_{H–H}$ = 8 Hz, $^2J_{Sn–H}$ = 55 Hz), 2.46 (tt, 6H, $^3J_{F–H}$ = 18 Hz, $^3J_{H–H}$ = 8 Hz); ^{19}F NMR (282.4 MHz, $CDCl_3$) δ – 81.10 (t, 9F), −116.28 (m, 6F), −124.41 (m, 6F), −126.09 (t, 6F); ^{13}C NMR (75 MHz, $CDCl_3$) δ 6.26 (s, $^1J_{C–Sn}$ = 190 Hz), 26.82 (t, $^2J_{C–F}$ = 23 Hz)*;* ^{119}Sn NMR (223.8 MHz, $CDCl_3$) δ 124.38.

HRMS (ESI^-) m/z theoretical for $C_{18}H_{12}Cl_2F_{27}Sn$ = 930.8904, found $[M+Cl]^-$ = 930.8895.

Fabrication of $CH_3NH_3PbI_3$ perovskite films. ITO substrates (1.5 × 1.5 cm^2) were cleaned by sonicating successively in deionized water with detergent, deionized water, and isopropanol for 10 min each. Then, the pre-cleaned ITO substrates were exposed to UV-ozone treatment for 15 min to reform the surface. After ozone cleaning, the ITO substrates were transferred to a nitrogen-filled glovebox to spin-coat the perovskite solution. The perovskite solution was prepared by dissolving 0.72 M $PbAc_2 \cdot 3H_2O$ (Merck) and 2.2 CH_3NH_3I (GreatCell Solar

Materials) in DMF (Merck) and stirring at room temperature for about 30 minutes. The solution was filtered with 0.4 μm PTFE filter and spin-coated at 6000 rpm for 2 min on top of the ITO substrates. The samples were dried at room temperature for 3 minutes, then annealed at 100^{o}C for 25 min. For PM-IRRAS experiments, the perovskite solution was spin-coated onto gold substrates.

Adlayer deposition. To deposit adlayers, 100 μL of the prepared solutions (10 mM in TFT or TL) were drop-casted on perovskite film and incubated for 2 min before spin-coating at 2000 rpm for 1 min, followed by rinsing with the corresponding solvent.

Material Characterization. The crystalline structure of the hybrid perovskite films was determined by X-ray diffraction (D2 PHASER, Bruker AXS) employing monochromatic Cu Kα radiation (λ = 1.54056 Å) and a current/voltage of 10 mA/30 kV. Scanning was carried out for 2θ ranging from 7 to 60° with a step of 0.01°. Surface chemical compositions were determined by XPS using a Thermo Fisher Scientific K-ALPHA spectrometer. Samples were freshly prepared on ITO substrates in a nitrogen-filled glovebox and sealed in a vacuum box to be introduced on the same day for the measurements. Films were analyzed with a monochromatized Al-Kα source (hν = 1486.6 eV) and a 400 μm X-Ray spot size. Three measurements per sample were carried out to ascertain the reproducibility of the surface chemistry. The survey spectra (0-1300 eV) were recorded using a constant pass energy of 200 eV, while high-resolution spectra were recorded with a continuous pass energy of 40 eV. Charge neutralization was applied during the analysis. High-resolution spectra (i.e. C1s, Pb4f, I3d, F1s, Sn3d, Cl2p, …) were quantified using the Avantage software provided by Thermo Fisher Scientific. Main attention was paid to F1s, Sn3d and Cl2p spectra by fitting to discuss the chemical bonding. Contact angle determinations for water were carried out on a Kruss DAS 100 apparatus (Drop Shape System DAS 10 Mk2) in

static mode at room temperature. The reported values correspond to the average of at least three measurements. The surface potential was measured in ambient condition by Kelvin probe technique using vibrating gold grid reference electrode (Kelvin probe S, Bescoke Delta Phi, diameter 2.5 mm). PM-IRRAS spectra of **1a**, **1b**, **2a**, **2b**, and **3** interfacial films deposited onto perovskite/gold substrates were recorded on a ThermoNicolet Nexus 670 FTIR spectrometer at a resolution of 4 cm^{-1}, by coadding eight blocks of 1500 scans (4 h total acquisition time). All spectra were collected in a controlled dry environment (relative humidity around 3%). Experiments were performed at an incidence angle of 75° using an external homemade goniometer reflection attachment and adding a ZnSe photoelastic modulator (PEM, Hinds Instruments, type III) after the polarizer.[37] For calibration measurements, a second linear polarizer (oriented parallel or perpendicular to the first preceding the PEM) was inserted between the sample and the second ZnSe lens. This procedure was used to calibrate and convert the PM-IRRAS signal in terms of the IRRAS signal (i.e., $1 - \frac{R_p(d)}{R_p(0)}$ where $R_p(d)$ and $R_p(0)$ stand for the p-polarized reflectance of the film/substrate and bare substrate systems, respectively).[38,39]

RESULTS AND DISCUSSION

Four fluorinated organotin compounds with different polarities were selected (Figure 1) to compare the effect of fluorine atom content and dipole moment on the material's work function, photoluminescence, and hydrophobicity. Compared to **1**, the Sn–Cl bond in **2** is expected to increase the overall dipole moment with respect to the more symmetrical tetraorganotin derivative. For each, two different lengths of perfluoalkyl chains were tested, either 1*H*, 1*H*, 2*H*, 2*H*-perfluorohexyl (**1a** and **2a**) or 1*H*, 1*H*, 2*H*, 2*H*-perfluorooctyl (**1b** and

2b). The C_4F_9 or C_6F_{13} groups provide fluorophilicity, while the C_2H_4 spacer improves the chemical stability by mitigating the electronic effect of the fluoroalkyl chain on the metal center. Additionally, tris(pentafluorophenyl)borane (**3**) was tested due to its strong dipole moment. The compounds were obtained by reacting the corresponding Grignard reagent RMgI (prepared via the reaction of RI with Mg) with tin tetrachloride.[40] For the monochlorinated tin compounds **2**, the corresponding R_3SnPh intermediate was obtained by adding phenyltin trichloride to an excess of RMgI,[41] followed by an electrophilic cleavage of the tin-phenyl bond under mild conditions using TMSCl.[40] The molecular structure of the products was confirmed by ^{1}H, ^{13}C, ^{19}F and ^{119}Sn NMR spectroscopy as detailed in the supporting information. In particular, ^{119}Sn chemical shifts of the various fluorinated organotins fall within the range of those reports for tetraalkyl-, phenyltrialkyl- and monochlorotrialkyltin analogues,[40,42] i.e. 10.8 ppm and 10.5 ppm for **1a** and **1b**, - 33.6 ppm and - 28.6 ppm for $(C_4F_9C_2H_4)_3SnPh$ and $(C_6F_{13}C_2H_4)_3SnPh$, 124.4 ppm and 124.0 ppm for **2a** and **2b**, respectively. Synthetic details and spectral characterization information are presented in the experimental section and supporting information.

To test the four fluorinated alkyltin compounds as interfacial adlayers, the latter were deposited by spin-coating a dilute solution (10 mM) from two different solvents, toluene (TL), or α,α,α-trifluorotoluene (TFT) on top of the $CH_3NH_3PbI_3$ surface. Then, the resulting layers were rinsed with pure solvent to remove excess material. To evaluate the influence of the perfluorinated molecules on the structure of the HOIP polymorph and the surface morphology, XRD and atomic force microscopy (AFM) measurements were performed on pristine and modified $CH_3NH_3PbI_3$ films. For all samples, the diffraction pattern of the XRD studies shows peaks at 14.1, 28.6, and 43.2° (2θ) attributed to the (110), (220), and (330) planes of a pure tetragonal perovskite structure.[43,44] A weak peak at 12.6° 2θ is also observed and attributed to the

(001) plane of traces of PbI_2 present in all the samples (Figure S29). These results confirm that no phase transformation occurs upon exposure to the solvent or depositing the perfluorinated molecules on top of the MAPI surface. The AFM results (Figure S30) were in line with the XRD measurements revealing negligible change in the surface morphology and roughness upon the adlayers deposition on top of the MAPI surface. The ultraviolet-visible (UV-vis) absorption spectra of the pristine and modified MAPI surfaces are primarily used to find any significant change in the energy band structure upon surface modification. As can be observed in Figure S31, the absorption edge was slightly blue-shifted upon ad-layer deposition in cases **2** and **3**. The band gap of the pristine MAPI, as determined from Tauc plot (1.56 eV), is in good agreement with the reported band gap.[45] After the ad-layer deposition, the band gap increases up to 1.58 eV for **2** (Table S1).

The presence and composition of the fluorinated interfacial layers were characterized by PM-IRRAS and XPS. The latter is beneficial in evidencing the existence of fluorinated species thanks to signals from F 1s orbitals. Control experiments with pristine perovskite films treated with neat TFT revealed no signals attributable to F atoms (Figure 2A and Figure S32), evidencing the absence of residual solvent molecules. On the other hand, for $CH_3NH_3PbI_3$ films coated with **1** or **2**, a clear emission line was detected at 688.2 ± 0.1 eV assigned to the F 1s core level (Figure 2B and D) and evidenced the presence of a thin perfluoroalkyl tin layer on top of the perovskite film. The deconvoluted F 1s spectrum contains two peaks representing CF_2 and CF_3 groups.[46,47] The CF_3 groups could be assigned to those peaks displaced at the highest binding energy as it was demonstrated elsewhere that surface fluorination had shifted the F peaks to a higher binding energy by increasing the F content with respect to the C one.[48,49] Moreover, for both **1b**/TFT and **2b**/TL-treated surfaces, the Sn $3d_{5/2}$ region exhibited a single feature at a

binding energy of 487.0 eV (Figure 2C) and 487.3 eV (Figure 2E), respectively, with a spin-orbit splitting of 8.3 ± 0.1 eV to Sn $3d_{3/2}$ indicating the presence of only Sn(IV) states with no noticeable Sn(II) nor Sn(0) which are expected at 485.8 eV and 484.5 eV, respectively.[50,51] An emission line at 198.5 ± 0.1 eV was detected in the Cl 2p region (Figure 2F), which is consistent with the presence of Sn-Cl bonds.[50,52,53] The absence of these signals for the **1a**/TL- and **2a**/TL-treated surfaces are assigned to low surface coverage, placing them beyond the detection limit of Sn and Cl core levels by XPS. For comparison, XPS measurements on **3**-treated surfaces reveal an F 1s peak at 688.2 eV ± 0.1 eV along with a B 1s peak at 186.6 eV ± 0.2 eV, coincidental with that of the I 4s peak (Figure S33). For all pristine and modified MAPI surfaces, the Pb 4f region shows two main features at 143.5 ± 0.1 and 138.7 ± 0.1 eV arising from the spin-orbit splitting of f-orbital and attributed to Pb $4f_{5/2}$ and Pb $4f_{7/2}$, respectively (Figure S32 and S33).[54] Both core level binding energies and spin-orbit splitting of 4.8 eV are consistent with Pb(II) sites in MAPI. A weak feature at low binding energy (about 137 eV) was also detected, which can be assigned to Pb(0), as previously reported in the literature.[55] Furthermore, the I 3d region confirms the formation of a neat MAPI layer with typical emissions at 631.1 ± 0.1 and 619.5 ± 0.1 eV assigned to I $3d_{3/2}$ and I $3d_{5/2}$ core levels (Figure S33).

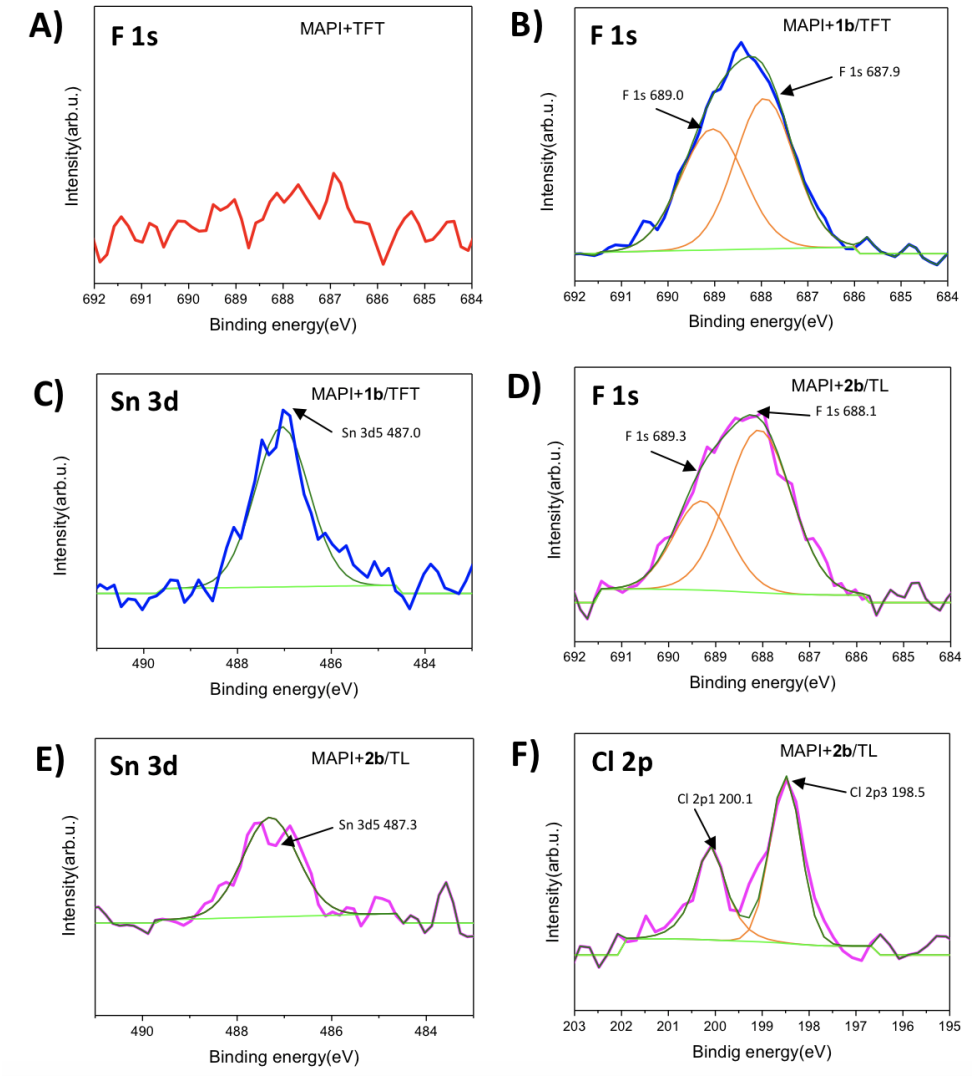

Figure 2. XPS spectra of fitted F 1s, Sn 3d or Cl 2p for (A) TFT-treated, (B, C) **1b**/TFT-treated and (D – F) **2b**/TL-treated MAPI surfaces.

In optimal cases, the orientation, thickness, and existence of specific interactions between the adlayer and the MAPI surface can be obtained using PM-IRRAS. This technique was previously reported by Sadhu *et al.*[25] to study surface-modified perovskite films deposited onto gold-coated glass slides. This provides vibrational spectra with an excellent signal-to-noise ratio over the 2000–800 cm^{-1} region that is of interest to visualize the methyl ammonium ions and the CF_2 vibrations of the perfluoroalkyl chain, as can be seen in Figure 3A. To reduce intramolecular

repulsion between vicinal CF_2 groups, perfluorinated chains adopt a zig-zag helical conformation.[56] Thus, the CF_2 vibrations group into modes that are either parallel to the helix axis (A_2 symmetry) or perpendicular to it (E_1 symmetry).[57,58] Interestingly, the results from the PM-IRRAS measurement of **1b**/TFT (Figure 3B) show strong contributions from the vibrational modes oriented perpendicular to the helix axis (bands at 1252, 1215, and 1147 cm^{-1}). Due to the selection rule of the PM-IRRAS (transition moment oriented parallel to the surface are not detected), this indicates that the perfluorinated chains are not isotropically oriented with respect to the surface but possess a horizontal arrangement as illustrated in Figure 1. From this, we may deduce that the compounds are tiled flat onto the perovskite surface rather than as an amorphous layer. On the other hand, the PM-IRRAS measurement of **2b**/TFT on MAPI (Figure 3C) reveals not only contributions of CF_2 groups from the vibrational modes oriented perpendicular to the helix axis (bands at 1248 and 1212 cm^{-1}) but also modes that are along the helix axis (bands at 1377 and 1361 cm^{-1}). These latter bands indicate that **2b**/TFT perfluorinated chains adopt a less parallel orientation to the MAPI surface than those observed for **1b** molecules. Finally, the contributions observed at 1587 and 1478 cm^{-1} arise from the difference in the broadness of the bands related to the asymmetric and symmetric bending vibrations of the NH_3^+ groups, respectively, between the treated and non-treated MAPI surfaces. These are likely due to specific interactions between molecules of **2** with the methyl ammonium groups of MAPI, certainly involving the Cl atom. The interactions between the CF_2 groups and the MAPI surface could generally originate from H-bonding between the fluorine and the methylammonium cations, possibly providing multi-point interactions between the fluoroalkyl chains and the underlying surface.[25]

The intensity of the PM-IRRAS signals depends on the quantity of molecules on the surface and their orientation. This allows the determination of not only the molecule orientation, but also the film thickness by simulating the experimental spectra from the material's isotropic optical constants determined using the *p*- and *s*-polarized attenuated total reflection (ATR) spectra of the films (Figure S35).[25] Generally, we observe low surface coverage resulting from rinsing the substrate after depositing the interfacial layer. This was done to remove excess material that would otherwise lie between the active layer and the electrode or interfacial layer, which could be detrimental to the electrical properties of a device. Also, fluorinated alkyl chains generally form less densely packed monolayers when compared to non-fluorinated ones.[59,60] The calculated values of average film thickness are given in Table 1 and show that samples treated with **1**/TFT form the most compact interfacial layers with a better surface coverage (ca. 6 Å). This likely corresponds to full surface coverage with one to two molecules retained after rinsing. In contrast, films of **2**/TFT and **3** give weaker spectral signatures consistent with molecular layers whose average thickness (ca. 1 Å) is less than that expected from a single molecule layer oriented horizontally on the surface. This is indicative of incomplete surface coverage under these deposition conditions. Control experiments in which the substrates were not rinsed following adlayer deposition possessed significantly greater thicknesses.

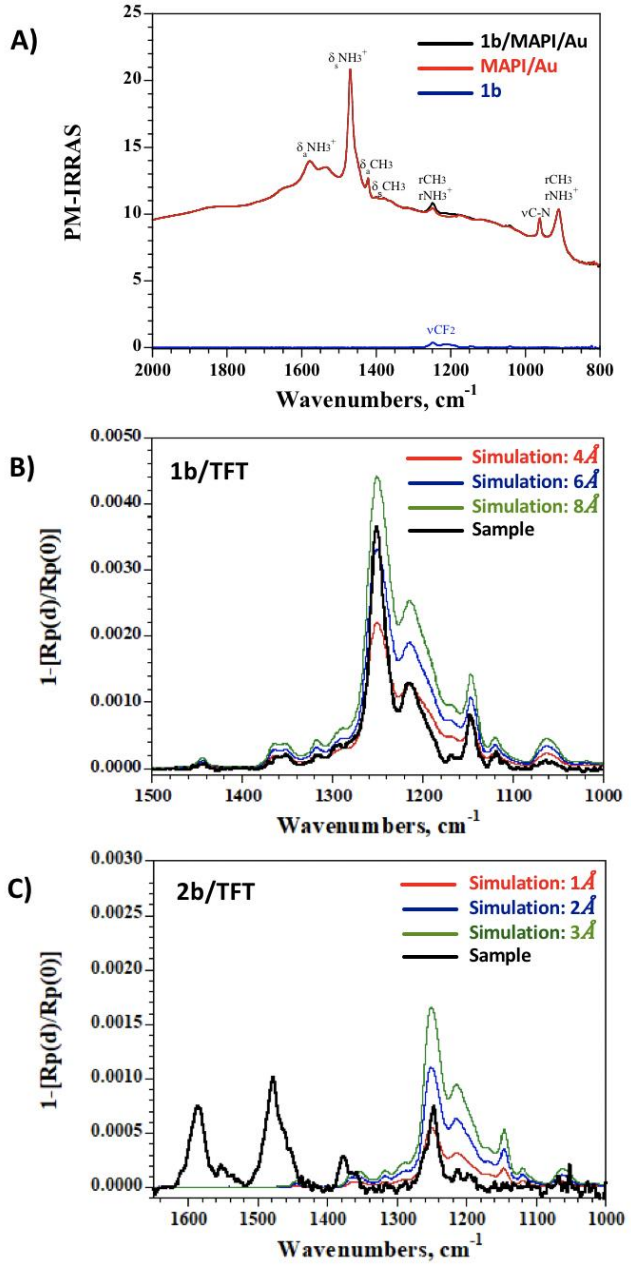

Figure 3. (A) PM-IRRAS spectra of pristine MAPI (red line) and after exposure to **1b** (black line). The baseline-corrected difference signal evidencing the CF_2 vibrations is shown in blue. (B), (C) Zoom-in of the PM-IRRAS spectrum of **1b**/TFT and **2b**/TFT modified perovskite surfaces (black lines). Also shown are simulated spectra of compact isotropic layers with different thicknesses calculated from the isotropic optical constants determined from ATR measurement (see supporting information).

Surface modification using the fluorinated derivatives is expected to cause an increase in the hydrophobicity of the perovskite layer. This can be directly probed using contact angle (CA) measurements and has previously been used by others to measure the interfacial layer's ability in protecting the perovskite from damage by moisture.[6] The CA for MAPI samples treated with **1** – **3** are shown in Table 1, Figure 1, and S34. The sample without any surface treatment shows a contact angle of ca. 40°, similar to that previously reported for untreated MAPI surfaces.[61] Interestingly, a modest increase in the contact angle is observed for samples treated with neat solvent (TL or TFT), indicating that some passivation or solvent-induced surface reorganization that increases the surface hydrophobicity takes place upon exposure to a hydrophobic solvent. The deposition of **1b**, having the longer fluorinated chain, leads to the strongest increase in surface hydrophobicity. Expectedly, using a shorter fluoroalkyl chain in **1a** leads to a smaller contact angle that is intermediate between that of the neat solvent and **1b**. It is surprising to note that, although an incomplete surface coverage with an average thickness of 1 Å is obtained when depositing **1a** from TL vs. TFT, a similar contact angle value is obtained for both solvents. This may suggest that the molecules deposited onto the surface preferentially bind to surface sites that are (partially) responsible for the substrate's overall hydrophilicity. By passivating these sites, an interfacial layer may thus substantially enhance the material's resistance to damage by moisture, even in the absence of a uniform hydrophobic film. A similar case is observed for **3**, which contains a substantially lower fluorous content with respect to **1a** and **1b** (55.6% vs. 61.8% and 65.6%, respectively). Despite a low surface coverage, a significant increase in surface hydrophobicity is observed with a contact angle reaching 76° when deposited from TFT. Finally, the more polar compounds **2** possess greater solubility in TL, and this solvent gives larger contact angle values with respect to neat solvent treatment than TFT (Table 1).

The interactions observed between the MAPI surface and the fluorinated adlayers were previously reported to modify the material's electronic properties.[25] These variations concern the interfacial layer and can be quantified by the work function (WF) of the modified surface. The latter can be evaluated using Kelvin probe measurements by comparison with a reference surface such as freshly cleaved highly ordered pyrolytic graphite (HOPG) with WF = 4.470 ± 0.005 V.[62]

The surface potential of pristine MAPI was determined to be 5.29 V, whereas that of the TFT and TL-treated samples was found to be lowered to 5.12 and 5.19 V, respectively (Table 1). This change in WF parallels the changes observed by contact angle measurement and supports the occurrence of some surface reorganization upon treatment with a neat solvent. Taking the WF value of the solvent-treated surfaces as a reference, we may compare the WF of the treated ones. The values collected in Table 1 show that all of the studied fluorinated compounds lead to an increase in the surface WF. The most significant enhancement (+230 mV) is observed for **2b** deposited from TL. Although the lower value for the same species from TFT might be due to its lower surface coverage, an inspection of the data in Table 1 reveals that all of the surfaces modified from TFT exhibit lower increases in WF with respect to the same compound deposited from TL. This confirms that the choice of solvent is crucial when considering the effect of surface modifiers for perovskite devices. In contrast, a comparison of the long and short fluoroalkyltin compounds evidences that, despite similar thickness and surface coverage, the effect of **1a** is smaller than that of **1b** (+50 mV vs. +170 mV, respectively). Examination of the PM-IRRAS signals shows that the shorter-chain **1a**/TFT derivative possesses a stronger contribution of the A_2 symmetry signal (Figure S36), suggesting that the molecular layer is less ordered than for **1b**/TFT. In support of this, we note that the situation is reversed in TL, where the fluorinated chains in **1a** are strongly oriented parallel to the surface and lead to an increase of

the WF of +210 mV despite a low surface coverage. We may therefore conclude that the WF modification situation is similar to that observed for the surface hydrophobicity in that it is not directly proportional to the amount of material deposited but rather to the compound's dipole moment and orientation and, presumably, its localization with respect to surface defects.

Table 1. Average work function, thickness and water contact angle of pristine and treated MAPI surfaces using either TFT or TL-based solutions. [a]

	TFT			TL		
	WF (V)	Average thickness (Å)[b]	Contact angle (°)	WF (V)	Average thickness (Å)[b]	Contact angle (°)
Pristine MAPI	5.29 ±0.02		39.6±2.5	5.29±0.02		39.6±2.5
MAPI + solvent	5.12±0.01		62.5±0.9	5.19±0.01		53.2±1.2
MAPI + **1a**	5.17±0.06	6	69.0±1.9	5.40±0.05	1	70.5±2.3
MAPI + **1b**	5.29±0.02	6	82.7±1.7	[c]	[c]	[c]
MAPI + **2a**	5.15±0.08	1	64.1±2.0	5.33±0.03	1	64.8±2.8
MAPI + **2b**	5.27±0.03	1	57.9±0.4	5.42±0.02	3	61.2±1.7
MAPI + **3**	5.22±0.03	1	76.0±1.9	5.39±0.02	1	60.7±1.0

[a] Deposited by spin-coating a 10 mM solution from either TFT or TL followed by rinsing the surface with neat solvent. Average of at least three measurements. [b] Estimated by PM-IRRAS. Values less than the molecular dimensions correspond to incomplete surface coverage. [c] Not soluble

Passivation of surface defects reduces trap-assisted Shockley-Read-Hall recombination processes[63] and is thus a significant contributing factor in optimizing the efficiency of PSCs. The effect of surface modification can be readily quantified from the photoluminescence efficiency (PLQE) and time-resolved decay (TRPL), as both of these are affected by the presence of surface defects.[64-66] Snaith and co-workers previously showed that the TRPL signals can be decomposed

according to a model in which fast bimolecular recombination is followed by a slower monoexponential decay characteristic of the concentration of trap states.[66,67] The impact of the presence of adlayers of **1** – **3** deposited from different solvents on the SRH recombination processes can be assessed by probing the steady-state and time-resolved photoluminescence (PL) properties of the samples along with the average lifetime of the luminescence decay.[68] The emission maximum, average lifetime (calculated from the multiexponential reconvolution of the luminescence decay), and quantum yield (PLQY) are given in Table 2 for pristine MAPI, MAPI treated with neat TFT or TL solvents, or with solutions of **1** – **3**.

Table 2. Photoluminescence quantum efficiency and time-resolved decay parameters for pristine MAPI and samples treated using either TFT or TL-based solutions.[a]

	TFT			TL		
	λ_{em} (nm)	τ_{avg} (ns)	PLQE (%)	λ_{em} (nm)	τ_{avg} (ns)	PLQE (%)
Pristine MAPI	774	313	0.26	774	313	0.26
MAPI + solvent	774	368	0.09	774	479	0.20
MAPI + **1a**	774	402	0.39	774	520	0.48
MAPI + **1b**	774	577	0.37	[b]	[b]	[b]
MAPI + **2a**	768	600	0.75	768	585	0.57
MAPI + **2b**	768	658	0.80	768	520	0.68
MAPI + **3**	774	544	0.60	774	473	0.24

[a]Measured using λ_{ex} = 456 nm (0.24 nJ/pulse) and λ_{em} = 760 nm. [b] not soluble

As shown in Figure 4A and Table 2, surface modification of MAPI films with molecules **1**, **2**, and **3** led to a significant increase in the PL intensity and photoluminescence quantum yield (PLQE), while simple solvent treatment of MAPI films with TFT or TL did not result in similar increase in PLQE. These results suggest that the number of trap states at the origin of non-

radiative recombination is decreased when **1**-, **2**- or **3**-adlayers are introduced. The fluorinated chlorotin compounds **2** yielded the most significant enhancement in PLQE, with values ranging from 0.57 to 0.8%, with a maximum for MAPI surface modified with **2b**/TFT. Interestingly, we note that PL emission occurs at 774 ± 1 nm for pristine MAPI, TFT or TL-treated MAPI, and **1**- or **3**-modified MAPI films, whereas MAPI treated with **2** exhibits a blue-shifted emission at 768 ± 1 nm. This is consistent with the slightly higher energy band gap determined for MAPI films treated with the tin chloride derivatives **2** (Figure S31 and Table S1) and suggests that chlorotin fluorocarbon derivatives possess an affinity for specific surface defect sites in MAPI. Specific interactions between **2** and the MAPI surface were also evidenced by the shift in the vibrational frequency of the NH_3^+ fragment observed in the PM-IRRAS spectra.

As expected, the TRPL decay of the samples was multi-exponential (Figure 4B) with a long-lived component comprised between 0.4 and 1 μs. The intensity-averaged lifetime was calculated for each sample (Table 2), confirming that the increase in PLQE is due to a reduction of the non-radiative recombination efficiency, especially in the case of polar chlorotin compounds **2**. Assuming that the radiative recombination rates are unaffected by surface passivation, one would expect a linear correlation between the enhancement in emission quantum yield and the increase in average lifetime of the samples. Despite some scatter in the data due to the difficulties in precisely determining PLQE and TRPL from solid samples with low emission, this is clearly the case, as shown in the inset to Figure 4B. What is most remarkable, in our opinion, is that the large differences in surface coverage observed between the treated samples (Table 1) do not appear to be a determining factor in the adlayer's ability to passivate surface defects as probed by PL measurements.

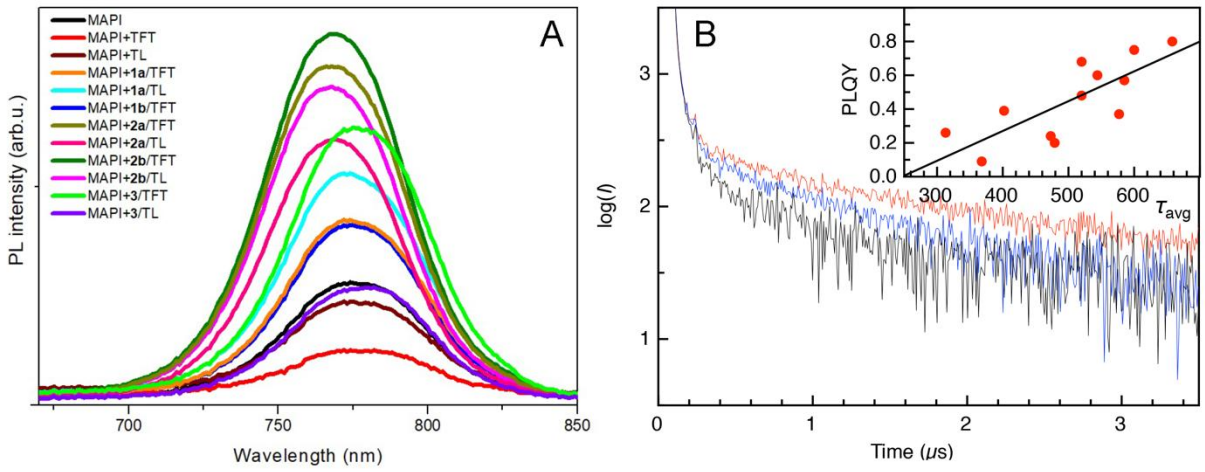

Figure 4. (A) PL spectra of pristine and modified MAPI surfaces (λ_{ex} = 365 nm). (B) TRPL decay (λ_{ex} = 456 nm (0.24 nJ/pulse), λ_{em} = 760 nm) of pristine MAPI surface (black), MAPI following treatment with neat toluene (blue), or with **2a** in toluene (red), Inset shows a correlation between the PLQY and average lifetime with black line representing best fit according to a linear regression (r^2 = 0.78).

CONCLUSION

The formation of fluorinated adlayers from tetra(fluoroalkyl)stannanes or chlorotri(fluoroalkyl)stannanes on top of MAPI was confirmed through XPS and PM-IRRAS measurements. The latter also provides information on the thickness and the orientation of the fluorinated chains, revealing that the amount and organization of the surface modifier left after rinsing was highly dependent on the nature of the fluorinated species and the solvent used for deposition. This, in turn, affects the overall properties of the material, which were highly sensitive to the ordering and molecular dipole moment rather than simply correlating with the amount of material deposited. From these results, we may tentatively conclude that passivation of specific surface sites (eg, defects or grain boundaries) may provide the largest contribution to altering the perovskite surface properties such as hydrophobicity and work function. For all compounds examined, XRD analyses confirm that the bulk crystallinity of the perovskite material is retained. In the most favorable case, a monomolecular layer surface coverage of **2b** is

sufficient to increase the material's WF by 230 mV, whereas a slightly thicker layer of **1b** provides the most significant increase in surface hydrophobicity. In contrast, the passivation of trap sites contributing to non-radiative charge recombination is not dependent on the full surface coverage by the passivating agent. This in turn confirms that specific interactions promote the deposition of the latter to defect sites that contribute to non-radiative recombination.

Our results also confirm the importance of the solvent chosen for the deposition of the passivating layer. Different WF and contact angle values are obtained when different solvents are used, and for both toluene and α,α,α-trifluorotoluene, exposure to these solvents alters the surface properties by decreasing the WF and increasing the hydrophobicity of the surface. We may thus conclude that understanding surface modification of hybrid perovskite materials is a complex undertaking that cannot be approximated by transposing the bulk properties of the interfacial layer. Instead, one must consider its molecular properties and ordering on the surface, as well as solvent effects.

ASSOCIATED CONTENT

Supporting Information

The Supporting Information is available free of charge at:

Additional experimental details for the synthesis of compounds **1 and 2** and their characterization, materials, and methods for PM-IRRAS, AFM, and XPS analyses.

AUTHOR INFORMATION

Corresponding Authors

Dario Bassani - *Univ. Bordeaux, CNRS, Bordeaux INP, ISM, UMR 5255, F-33400 Talence, France. E-mail: dario.bassani@u-bordeaux.fr*

Thierry Toupance - *Univ. Bordeaux, CNRS, Bordeaux INP, ISM, UMR 5255, F-33400 Talence, France. E-mail: thierry.toupance@u-bordeaux.fr*

Author Contributions

The manuscript was written through contributions of all authors. All authors have given approval to the final version of the manuscript.

Notes

The authors declare no competing financial interests.

ACKNOWLEDGMENT

The Agence Nationale de la Recherche (HYPERSOL project no. ANR-18-CE05-0021-01) and the Region Nouvelle Aquitaine (STRIPE project no. 2019-1R1M08) are gratefully acknowledged for their financial support. This work also benefited from the facilities and expertise of CESAMO platform, UMR 5255 supported by the Aquitaine government.

REFERENCES

(1) De Wolf, S.; Holovsky, J.; Moon, S.-J.; Löper, P.; Niesen, B.; Ledinsky, M.; Haug, F.-J.; Yum, J.-H.; Ballif, C. Organometallic Halide Perovskites: Sharp Optical Absorption Edge and Its Relation to Photovoltaic Performance. *J. Phys. Chem. Lett.* **2014**, *5*, 1035-1039.

(2) Fakharuddin, A.; De Rossi, F.; Watson, T. M.; Schmidt-Mende, L.; Jose, R. Research Update: Behind the high efficiency of hybrid perovskite solar cells. *APL Mater.* **2016**, *4*, 091505.

(3) Herz, L. M. Charge-Carrier Mobilities in Metal Halide Perovskites: Fundamental Mechanisms and Limits. *ACS Energy Lett.* **2017**, *2*, 1539-1548.

(4) Yun, S. N.; Qin, Y.; Uhl, A. R.; Vlachopoulos, N.; Yin, M.; Li, D. D.; Han, X. G.; Hagfeldt, A. New-generation integrated devices based on dye-sensitized and perovskite solar cells. *Energy Environ. Sci.* **2018**, *11*, 476-526.

(5) Park, J.; Kim, J.; Yun, H.-S.; Paik, M. J.; Noh, E.; Mun, H. J.; Kim, M. G.; Shin, T. J.; Seok, S. I. Controlled growth of perovskite layers with volatile alkylammonium chlorides. *Nature* **2023**, *616*, 724-730.

(6) Wolff, C. M.; Canil, L.; Rehermann, C.; Ngoc Linh, N.; Zu, F.; Ralaiarisoa, M.; Caprioglio, P.; Fiedler, L.; Stolterfoht, M.; Kogikoski, S.; Bald, I.; Koch, N.; Unger, E. L.; Dittrich, T.; Abate, A.; Neher, D. Perfluorinated Self-Assembled Monolayers Enhance the Stability and Efficiency of Inverted Perovskite Solar Cells. *ACS Nano* **2020**, *14*, 1445-1456.

(7) Jiang, Q.; Zhao, Y.; Zhang, X.; Yang, X.; Chen, Y.; Chu, Z.; Ye, Q.; Li, X.; Yin, Z.; You, J. Surface passivation of perovskite film for efficient solar cells. *Nat. Photon.* **2019**, *13*, 460-466.

(8) Li, L.; Lv, Y.; Liu, Q.; Fan, Z.; Yuan, R.; Tang, W.; Liu, X.; Zhang, P.; Zhang, W.-H. Efficient MA-free perovskite solar cells with balanced carrier transport achieved using 4-trifluorophenylammonium iodide. *J. Mater. Chem. A* **2022**, *10*, 9161-9170.

(9) Wang, H.; Zou, W.; Ouyang, Y.; Deng, X.; Luo, H.; Xu, J.; Liu, X.; Li, H.; Gong, X.; Lei, Y.; Ni, Y.; Peng, Y. Consolidating a Pb–X framework via multifunctional passivation with fluorinated zwitterions for efficient and stable perovskite solar cells. *J. Mater. Chem. A* **2022**, *10*, 10750-10758.

(10) Wu, T.; Li, X.; Qi, Y.; Zhang, Y.; Han, L. Defect Passivation for Perovskite Solar Cells: from Molecule Design to Device Performance. *ChemSusChem* **2021**, *14*, 4354-4376.

(11) Wang, S.; Wang, A.; Deng, X.; Xie, L.; Xiao, A.; Li, C.; Xiang, Y.; Li, T.; Ding, L.; Hao, F. Lewis acid/base approach for efficacious defect passivation in perovskite solar cells. *J. Mater. Chem. A* **2020**, *8*, 12201-12225.

(12) Gharibzadeh, S.; Abdollahi Nejand, B.; Jakoby, M.; Abzieher, T.; Hauschild, D.; Moghadamzadeh, S.; Schwenzer, J. A.; Brenner, P.; Schmager, R.; Haghighirad, A. A.; Weinhardt, L.; Lemmer, U.; Richards, B. S.; Howard, I. A.; Paetzold, U. W. Record Open-Circuit Voltage Wide-Bandgap Perovskite Solar Cells Utilizing 2D/3D Perovskite Heterostructure. *Adv. Energy Mater.* **2019**, *9*, 1803699.

(13) Yang, Z.; Dou, J.; Kou, S.; Dang, J.; Ji, Y.; Yang, G.; Wu, W.-Q.; Kuang, D.-B.; Wang, M. Multifunctional Phosphorus-Containing Lewis Acid and Base Passivation Enabling Efficient and Moisture-Stable Perovskite Solar Cells. *Adv. Funct. Mater.* **2020**, *30*, 1910710.

(14) Wang, F.; Bai, S.; Tress, W.; Hagfeldt, A.; Gao, F. Defects engineering for high-performance perovskite solar cells. *NPJ Flex. Electron.*. **2018**, *2*, 22-22.

(15) Pereyra, C.; Xie, H.; Lira-Cantu, M. Additive engineering for stable halide perovskite solar cells. *J. Energy Chem.* **2021**, *60*, 599-634.

(16) Zhang, H.; Chen, H.; Stoumpos, C. C.; Ren, J.; Hou, Q.; Li, X.; Li, J.; He, H.; Lin, H.; Wang, J.; Hao, F.; Kanatzidis, M. G. Thiazole-Induced Surface Passivation and Recrystallization of CH3NH3PbI3 Films for Perovskite Solar Cells with Ultrahigh Fill Factors. *ACS Appl. Mater. Interfaces.* **2018**, *10*, 42436-42443.

(17) Li, X.; Chen, C.-C.; Cai, M.; Hua, X.; Xie, F.; Liu, X.; Hua, J.; Long, Y.-T.; Tian, H.; Han, L. Efficient Passivation of Hybrid Perovskite Solar Cells Using Organic Dyes with -COOH Functional Group. *Adv. Energy Mater.* **2018**, *8*, 1800715.

(18) Zheng, X.; Chen, B.; Dai, J.; Fang, Y.; Bai, Y.; Lin, Y.; Wei, H.; Zeng, Xiao C.; Huang, J. Defect passivation in hybrid perovskite solar cells using quaternary ammonium halide anions and cations. *Nat. Energy* **2017**, *2*, 17102.

(19) Huang, W.; Manser, J. S.; Kamat, P. V.; Ptasinska, S. Evolution of Chemical Composition, Morphology, and Photovoltaic Efficiency of CH3NH3PbI3 Perovskite under Ambient Conditions. *Chem. Mater.* **2016**, *28*, 303-311.

(20) Wang, Y.; Zhang, T.; Kan, M.; Li, Y.; Wang, T.; Zhao, Y. Efficient α-CsPbI₃ Photovoltaics with Surface Terminated Organic Cations. *Joule* **2018**, *2*, 2065-2075.

(21) Xiao, K.; Han, Q.; Gao, Y.; Gu, S.; Luo, X.; Lin, R.; Zhu, J.; Xu, J.; Tan, H. Simultaneously enhanced moisture tolerance and defect passivation of perovskite solar cells with cross-linked grain encapsulation. *J. Energy Chem.* **2021**, *56*, 455-462.

(22) Sadhu, S.; Buffeteau, T.; Sandrez, S.; Hirsch, L.; Bassani, D. M. Observing the Migration of Hydrogen Species in Hybrid Perovskite Materials through D/H Isotope Exchange. *J. Am. Chem. Soc.* **2020**, *142*, 10431 – 10437.

(23) Zhou, Y.; Zhong, H.; Han, J.; Tai, M.; Yin, X.; Zhang, M.; Wu, Z.; Lin, H. Synergistic effect of charge separation and defect passivation using zinc porphyrin dye incorporation for efficient and stable perovskite solar cells. *J. Mater. Chem. A* **2019**, *7*, 26334-26341.

(24) Su, H.; Wu, T.; Cui, D.; Lin, X.; Luo, X.; Wang, Y.; Han, L. The Application of Graphene Derivatives in Perovskite Solar Cells. *Small Methods* **2020**, *4*, 2000507.

(25) Sadhu, S.; Aqueche, K.; Buffeteau, T.; Vincent, J. M.; Hirsch, L.; Bassani, D. M. Unexpected surface interactions between fluorocarbons and hybrid organic inorganic perovskites evidenced by PM-IRRAS and their application towards tuning the surface potential. *Mater. Horiz.* **2019**, *6*, 192-197.

(26) Azmi, R.; Zhumagali, S.; Bristow, H.; Zhang, S.; Yazmaciyan, A.; Pininti, A. R.; Utomo, D. S.; Subbiah, A. S.; De Wolf, S. Moisture-Resilient Perovskite Solar Cells for Enhanced Stability. *Adv. Mater.* **2023**, e2211317.

(27) Gassara, M.; Hemasiri, N. H.; Kazim, S.; Costantino, F.; Naili, H.; Ahmad, S. Uncovering the Role of Electronic Doping in Lead-free Perovskite (CH3NH3)2CuCl4-xBrx and Solar Cells Fabrication. *ChemSusChem* **2023**, e202202313.

(28) Liu, X.; Qiao, Y.; Guo, X. Roles that Organic Ammoniums Play on the Surface of the Perovskite Film: A Review. *Chem. - Eur. J.* **2023**, *29*, e202203001.

(29) Qiu, L.; Si, G.; Bao, X.; Liu, J.; Guan, M.; Wu, Y.; Qi, X.; Xing, G.; Dai, Z.; Bao, Q.; Li, G. Interfacial engineering of halide perovskites and two-dimensional materials. *Chem. Soc. Rev.* **2023**, *52*, 212-247.

(30) Raoui, Y.; Pegu, M.; Kazim, S.; Ahmad, S. Interfacial modification of perovskite solar cells via Cs2CO3: Computational and experimental approach. *Sol. Energy* **2021**, *228*, 700-705.

(31) Haris, M. P. U.; Xia, J.; Kazim, S.; Molenda, Z.; Hirsch, L.; Buffeteau, T.; Bassani, D. M.; Nazeeruddin, M. K.; Ahmad, S. Probing proton diffusion as a guide to environmental stability in powder-engineered FAPbI3 and CsFAPbI3 perovskites. *Cell Rep. Phys. Sci.* **2023**, *4*, 101304.

(32) Pegu, M.; Ghaderian, A.; Ahmad, S.; Kazim, S. Reducing the Trap Density in MAPbI3 Based Perovskite Solar Cells via Bromide Substitution. *ChemPlusChem* **2022**, *87*, e202200021.

(33) Jiang, X.; Chen, S.; Li, Y.; Zhang, L.; Shen, N.; Zhang, G.; Du, J.; Fu, N.; Xu, B. Direct Surface Passivation of Perovskite Film by 4-Fluorophenethylammonium Iodide toward Stable and Efficient Perovskite Solar Cells. *ACS Appl. Mater. Interfaces.* **2021**, *13*, 2558-2565.

(34) Pegu, M.; Kazim, S.; Buffeteau, T.; Bassani, D. M.; Ahmad, S. Deciphering the Orientation of the Aromatic Spacer Cation in Bilayer Perovskite Solar Cells through Spectroscopic Techniques. *ACS Appl. Mater. Interfaces.* **2021**, *13*, 48219-48227.

(35) Rusu, P. C.; Brocks, G. Surface Dipoles and Work Functions of Alkylthiolates and Fluorinated Alkylthiolates on Au(111). *J. Phys. Chem. B* **2006**, *110*, 22628-22634.

(36) Gobbi, M.; Orgiu, E.; Samorì, P. When 2D Materials Meet Molecules: Opportunities and Challenges of Hybrid Organic/Inorganic van der Waals Heterostructures. *Adv. Mater.* **2018**, *30*, 1706103.

(37) Buffeteau, T.; Desbat, B.; Turlet, J. M. Polarization Modulation FT-IR Spectroscopy of Surfaces and Ultra-Thin Films: Experimental Procedure and Quantitative Analysis. *Applied Spectroscopy* **1991**, *45*, 380-389.

(38) Buffeteau, T.; Desbat, B.; Blaudez, D.; Turlet, J. M. Calibration procedure to derive IRRAS spectra from PM-IRRAS spectra. *Applied Spectroscopy* **2000**, *54*, 1646-1650.

(39) Ramin, M. A.; Le Bourdon, G.; Daugey, N.; Bennetau, B.; Vellutini, L.; Buffeteau, T. PM-IRRAS Investigation of Self-Assembled Monolayers Grafted onto SiO2/Au Substrates. *Langmuir* **2011**, *27*, 6076-6084.

(40) Imakura, Y.; Nishiguchi, S.; Orita, A.; Otera, J. Assessment of fluoroalkyltin compounds as fluorous Lewis acid catalysts. *Appl. Organomet. Chem.* **2003**, *17*, 795-799.

(41) Curran, D. P.; Hoshino, M. Stille Couplings with Fluorous Tin Reactants: Attractive Features for Preparative Organic Synthesis and Liquid-Phase Combinatorial Synthesis. *J. Org. Chem.* **1996**, *61*, 6480-6481.

(42) Wrackmeyer, B. In *Annual Reports on NMR Spectroscopy*; Webb, G. A., Ed.; Academic Press: 1999; Vol. 38, p 203-264.

(43) Noel, N. K.; Abate, A.; Stranks, S. D.; Parrott, E. S.; Burlakov, V. M.; Goriely, A.; Snaith, H. J. Enhanced Photoluminescence and Solar Cell Performance via Lewis Base Passivation of Organic–Inorganic Lead Halide Perovskites. *ACS Nano* **2014**, *8*, 9815-9821.

(44) Huang, W.; Manser, J. S.; Sadhu, S.; Kamat, P. V.; Ptasinska, S. Direct Observation of Reversible Transformation of CH3NH3PbI3and NH4PbI3Induced by Polar Gaseous Molecules. *J. Phys. Chem. Lett.* **2016**, *7*, 5068-5073.

(45) Gallet, T.; Grabowski, D.; Kirchartz, T.; Redinger, A. Fermi-level pinning in methylammonium lead iodide perovskites. *Nanoscale* **2019**, *11*, 16828-16836.

(46) Boutet, S.; Jousseaume, B.; Toupance, T.; Biesemans, M.; Willem, R.; Labrugère, C.; Delattre, L. Functionalization of Silica Gel with Organotrialkynyltins: New Method of Covalent Attachment of Organic Groups on Silica Gel. *Chem. Mater.* **2005**, *17*, 1803-1811.

(47) Wang, K.-T.; Wang, W.-Y.; Wei, T.-C. Photomask-Free, Direct Selective Electroless Deposition on Glass by Controlling Surface Hydrophilicity. *ACS Omega* **2019**, *4*, 7706-7710.

(48) Shirasaki, T.; Moguet, F.; Lozano, L.; Tressaud, A.; Nanse, G.; Papirer, E. Fluorination of carbon blacks: an X-ray photoelectron spectroscopy study: IV. Reactivity of different carbon blacks in CF4 radiofrequency plasma. *Carbon* **1999**, *37*, 1891-1900.

(49) Durand, E.; Labrugère, C.; Tressaud, A.; Renaud, M. Surface Fluorination of Carboxylated Nitrile Butadiene Rubber: An XPS Study. *Plasmas Polym.* **2002**, *7*, 311-325.

(50) Moulder, J. F.; Stickle, W. F.; Sobol, P. E.; Bomben, K. D. *Handbook of X Ray Photoelectron Spectroscopy: A Reference Book of Standard Spectra for Identification and Interpretation of Xps Data* Perkin-Elmer Corporation, Physical Electronics Division: Eden Prairie, Minnesota, USA, 1992.

(51) Kwoka, M.; Ottaviano, L.; Passacantando, M.; Santucci, S.; Czempik, G.; Szuber, J. XPS study of the surface chemistry of L-CVD SnO2 thin films after oxidation. *Thin Solid Films* **2005**, *490*, 36-42.

(52) Félix, R.; Llobera-Vila, N.; Hartmann, C.; Klimm, C.; Hartig, M.; Wilks, R. G.; Bär, M. Preparation and in-system study of SnCl2 precursor layers: towards vacuum-based synthesis of Pb-free perovskites. *RSC Adv.* **2018**, *8*, 67-73.

(53) Grigas, J.; Talik, E.; Lazauskas, V.; Vysochanskii, Y. M.; Yevych, R.; Adamiec, M.; Nelkinas, V. XPS of Electronic Structure of Ferroelectric Sn2P2S6 Crystals. *Ferroelectrics* **2009**, *378*, 70-78.

(54) Philippe, B.; Park, B.-W.; Lindblad, R.; Oscarsson, J.; Ahmadi, S.; Johansson, E. M. J.; Rensmo, H. Chemical and Electronic Structure Characterization of Lead Halide Perovskites and Stability Behavior under Different Exposures—A Photoelectron Spectroscopy Investigation. *Chem. Mater.* **2015**, *27*, 1720-1731.

(55) Lin, W.-C.; Lo, W.-C.; Li, J.-X.; Wang, Y.-K.; Tang, J.-F.; Fong, Z.-Y. In situ XPS investigation of the X-ray-triggered decomposition of perovskites in ultrahigh vacuum condition. *NPJ Mater. Degrad.* **2021**, *5*, 13.

(56) Bunn, C. W.; Howells, E. R. Structures of Molecules and Crystals of Fluoro-Carbons. *Nature* **1954**, *174*, 549.

(57) Zenasni, O.; Jamison, A. C.; Marquez, M. D.; Lee, T. R. Self-assembled monolayers on gold generated from terminally perfluorinated alkanethiols bearing propyl vs. ethyl hydrocarbon spacers. *J. Fluorine Chem.* **2014**, *168*, 128-136.

(58) Lenk, T. J.; Hallmark, V. M.; Hoffmann, C. L.; Rabolt, J. F.; Castner, D. G.; Erdelen, C.; Ringsdorf, H. Structural Investigation of Molecular Organization in Self-Assembled Monolayers of a Semifluorinated Amidethiol. *Langmuir* **1994**, *10*, 4610-4617.

(59) Lorenz, C. D.; Webb, E. B.; Stevens, M. J.; Chandross, M.; Grest, G. S. Frictional dynamics of perfluorinated self-assembled monolayers on amorphous SiO2. *Tribol. Lett.* **2005**, *19*, 93-98.

(60) Liu, G. y.; Fenter, P.; Chidsey, C. E. D.; Ogletree, D. F.; Eisenberger, P.; Salmeron, M. An unexpected packing of fluorinated n-alkane thiols on Au(111): A combined atomic force microscopy and x-ray diffraction study. *J. Chem. Phys.* **1994**, *101*, 4301-4306.

(61) Yang, S.; Wang, Y.; Liu, P.; Cheng, Y.-B.; Zhao, H. J.; Yang, H. G. Functionalization of perovskite thin films with moisture-tolerant molecules. *Nat. Energy* **2016**, *1*, 15016.

(62) Hansen, W. N.; Hansen, G. J. Standard reference surfaces for work function measurements in air. *Surface Science* **2001**, *481*, 172-184.

(63) Kirchartz, T.; Márquez, J. A.; Stolterfoht, M.; Unold, T. Photoluminescence-Based Characterization of Halide Perovskites for Photovoltaics. *Adv. Energy Mater.* **2020**, *10*, 1904134.

(64) Bowman, A. R.; Macpherson, S.; Abfalterer, A.; Frohna, K.; Nagane, S.; Stranks, S. D. Extracting Decay-Rate Ratios From Photoluminescence Quantum Efficiency Measurements in Optoelectronic Semiconductors. *Phys. Rev. Appl.* **2022**, *17*, 044026.

(65) Ye, K.; Zhao, B.; Diroll, B. T.; Ravichandran, J.; Jaramillo, R. Time-resolved photoluminescence studies of perovskite chalcogenides. *Faraday Discuss.* **2022**, *239*, 146-159.

(66) de Quilettes, D. W.; Vorpahl, S. M.; Stranks, S. D.; Nagaoka, H.; Eperon, G. E.; Ziffer, M. E.; Snaith, H. J.; Ginger, D. S. Impact of microstructure on local carrier lifetime in perovskite solar cells. *Science* **2015**, *348*, 683 LP-- 686.

(67) Stranks, S. D.; Burlakov, V. M.; Leijtens, T.; Ball, J. M.; Goriely, A.; Snaith, H. J. Recombination Kinetics in Organic-Inorganic Perovskites: Excitons, Free Charge, and Subgap States. *Phys. Rev. Appl.* **2014**, *2*, 034007.

(68) Cheng, H.; Feng, Y.; Fu, Y.; Zheng, Y.; Shao, Y.; Bai, Y. Understanding and minimizing non-radiative recombination losses in perovskite light-emitting diodes. *J. Mater. Chem. C* **2022**, *10*, 13590-13610.